



HAL
open science

Bennu's near-Earth lifetime of 1.75 million years inferred from craters on its boulders

R.-L Ballouz, K J Walsh, Olivier Barnouin, D N Dellagiustina, M Al Asad, E
R Jawin, M G Daly, W F Bottke, Patrick Michel, C Avdellidou, et al.

► **To cite this version:**

R.-L Ballouz, K J Walsh, Olivier Barnouin, D N Dellagiustina, M Al Asad, et al.. Bennu's near-Earth lifetime of 1.75 million years inferred from craters on its boulders. *Nature*, 2020, 587, pp.205-209. 10.1038/s41586-020-2846-z . hal-03080437

HAL Id: hal-03080437

<https://hal.science/hal-03080437>

Submitted on 17 Dec 2020

HAL is a multi-disciplinary open access archive for the deposit and dissemination of scientific research documents, whether they are published or not. The documents may come from teaching and research institutions in France or abroad, or from public or private research centers.

L'archive ouverte pluridisciplinaire **HAL**, est destinée au dépôt et à la diffusion de documents scientifiques de niveau recherche, publiés ou non, émanant des établissements d'enseignement et de recherche français ou étrangers, des laboratoires publics ou privés.

Title: Bennu’s near-Earth lifetime of 1.75 million years inferred from craters on its boulders

Authors: R.-L. Ballouz^{1*}, K.J. Walsh², O.S. Barnouin³, D.N. DellaGiustina¹, M. Al Asad⁴, E.R. Jawin⁵, M.G. Daly⁹, W.F. Bottke², P. Michel⁶, C. Avdellidou⁶, M. Delbo⁶, R.T. Daly³, E. Asphaug¹, C.A. Bennett¹, E.B. Bierhaus⁷, H.C. Connolly Jr.^{8,1}, D.R. Golish¹, J.L. Molaro¹⁰, M. C. Nolan¹, M. Pajola¹¹, B. Rizk¹, S.R. Schwartz¹, D. Trang¹², C.W.V. Wolner¹, D.S. Lauretta¹.

Affiliations :

¹Lunar and Planetary Laboratory, University of Arizona, Tucson, AZ, USA,

²Southwest Research Institute, Boulder, CO, USA,

³The Johns Hopkins University Applied Physics Laboratory, Laurel, MD, USA,

⁴University of British Columbia, Vancouver, Canada,

⁵Smithsonian Institution, Washington, DC, USA,

⁶Laboratoire Lagrange, Université Côte d’Azur, Observatoire de la Côte d’Azur, CNRS, Nice, France,

⁷Lockheed Martin Space, Littleton, CO, USA,

⁸Dept. of Geology, Rowan University, Glassboro, NJ, USA,

⁹York University, Toronto, Canada,

¹⁰Planetary Science Institute, Tucson, AZ, USA,

¹¹INAF-Astronomical Observatory of Padova, Padova, Italy,

¹²HIGP/University of Hawaii at Manoa, HI, USA.

*Correspondence to: rballouz@orex.lpl.arizona.edu (R.-L.B.)

An asteroid’s history is determined in large part by its strength against collisions with other objects (impact strength) [1,2]. Laboratory experiments on centimeter-scale meteorites [3] have been extrapolated and buttressed with numerical simulations to derive the impact strength at the asteroid scale [4,5]. In situ evidence of impact processing of boulders on airless planetary bodies have come from Apollo lunar samples [6] and images of the asteroid (25143) Itokawa [7]. However, it has not been possible to directly assess the impact strength, and thus the absolute surface age, of the boulders that constitute the building blocks of a rubble-pile asteroid. Here we report an analysis of the size and depth of craters observed on boulders on the asteroid (101955) Bennu. We show that the impact strength of meter-sized boulders is 0.44 to 1.7 megapascals, which is weak compared to solid terrestrial materials. We infer that Bennu’s meter-sized boulders record its history of impact by millimeter- to centimeter-scale objects in near-Earth space. We conclude that this population of near-Earth impactors has a size frequency distribution similar to that of meter-scale bolides and originates from the asteroidal population. Our results indicate that Bennu has been dynamically decoupled from the main asteroid belt for 1.75 ± 0.75 million years.

We studied images of asteroid Bennu taken by the PolyCam instrument, part of the OSIRIS-REx Camera Suite (OCAMS) [8] onboard the Origins, Spectral Interpretation, Resource Identification, and Security–Regolith Explorer (OSIRIS-REx) spacecraft. These images resolved circular cavities that we interpret as craters with diameters, D_C , between 0.03 and 5 m, on boulders with diameters between 0.5 and 50 m (Fig. 1a-c). These images are divided into two datasets that differ in resolution and thus in resolvable crater size [9].

In the higher-resolution image set (1–3 cm/pixel), we mapped craters with $D_C < 50$ cm on boulders 0.5 to 2.5 m in diameter. These craters appear as impact pits on the flat faces of smooth boulders (Fig. 1a) and are difficult to observe on the surfaces of boulders with rougher surfaces. Nearly all flat, smooth boulder surfaces in this dataset have evidence of multiple impact pits. The interiors of the pits are typically shadowed. We therefore used data collected by the OSIRIS-REx Laser Altimeter (OLA) [10] to measure the depths of the largest pits in this set, those between 30 and 50 cm (of which there are six). We find depth, d , to diameter ratios, d/D_C , of approximately 0.25 (Fig. 1d).

In the lower-resolution image set (~ 5 cm/pixel), we mapped craters with $50 \text{ cm} < D_C < 5$ m on boulders ~ 1 to 50 m in diameter. Craters on the smaller end of this size range (0.5 to 1 m) occur on the surfaces of relatively flat boulders (Fig. 1b), whereas larger craters (1 to 5 m) are apparent on both flat and rough boulders (Fig. 1c). Typically, one to three craters are observable on a given boulder in this dataset.

Using OLA data, we measured $d/D_C = 0.33 \pm 0.08$ for a subset of craters measured in the lower-resolution images. These craters are large relative to their host boulder (ED Fig. 1 and ED Table 1) with crater-to-boulder diameter ratios greater than 0.3. The largest craters on boulders appear to have relatively flat floors and steep walls, compared to classic bowl-shaped craters. The crater interiors appear roughly textured in their OLA-derived profiles, and the images show decimeter-sized particulates overlaying the crater floors (Fig. 1c).

The largest craters relative to the host boulders may represent the largest sub-disruption impact sizes allowable. Laboratory impact experiments show that this is possible for impacts onto porous targets [11]; however, the largest possible craters on non-porous consolidated targets, produced through spall (fracturing and ejection of plate-like near-surface fragments), are created by impacts that are a factor of a few less than the disruption threshold [12]. Therefore, equating the formation of the largest possible crater to the catastrophic disruption threshold is a viable framework, as CM and CI meteorites—the meteoritic analogs to Bennu’s boulders—have high porosities ($\gtrsim 20\%$ [13]) and Bennu’s boulders show little evidence for spalls.

The specific impact energy, Q_D^* , required to disrupt an object with radius, R_T , at an impact speed of U , is given by $Q_D^* = q_S R_T^{-\mu_S} U^{2-3\mu_S} + q_G R_T^{3\mu_G} U^{2-3\mu_G}$ (see Methods Section 1.1.). The first term of the right side of the equation defines the target’s material strength against disruption, and the second term defines the energy required to overcome the target’s self-gravity. The first term typically dominates for small objects up to a few hundred meters, whereas the second dominates for larger objects. The material constants q_S and q_G set the scale of the catastrophic disruption threshold in the strength and gravity regimes, respectively. The dimensionless material constants

μ_S and μ_G set the size and velocity dependency of Q_D^* and define how energy and momentum from the projectile are coupled to the target [14].

The gravity regime parameters can be estimated from the results of numerical simulations and spacecraft observations of large asteroids (see Methods Eq. (M22-M23)). The value of μ_S is determined by considering an impact that delivers a specific impact energy that is just below that required by the disruption threshold. This forms a crater with radius $R_C = R_{C,\max}$, where $R_{C,\max}$ is the maximum possible crater radius. We measured the largest craters on Bennu’s boulder in the lower-resolution global dataset (Fig. 2, Supplementary Information Table 1). By comparing the values of $R_{C,\max}/R_T$ to R_T , we find $\mu_S = 0.47 \pm 0.07$. This value of μ_S is slightly larger than that determined from laboratory impact experiments into weakly cemented basalt and highly porous gypsum, which have $\mu_S = 0.46$ [15] and 0.4 [16], respectively. Then, the value of q_S is found by setting the transition diameter between the strength and gravity regime to the size of the largest observed monolithic C-complex object: the boulder Otohime on asteroid (162173) Ryugu, which has a diameter of 160 m [17] (see Methods Eq. (M24-M26)).

Using the derived prescriptions for the catastrophic disruption parameters, Fig. 3a compares Q_D^* for monolithic C-complex objects at typical main belt impact speeds, $U = 5$ km/s [2] with simulation results [4,5] for disruption against basalt and pumice targets. We find that monolithic C-complex targets are weaker than pumice and basalt targets of the same size. For example, Bennu’s 1-m-radius boulders require a factor of 4 to 10 less specific impact energy to disrupt than 1-m-radius basalt and pumice boulders. The values of Q_D^* measured for basalt and pumice were for oblique impacts, which lead to higher Q_D^* , as demonstrated in laboratory impact experiments [18]. Furthermore, we find that 1-cm radius targets have a $Q_D^* = 1.1 \times 10^7 - 3.0 \times 10^7$ erg/g, which is comparable to experimentally determined values of Q_D^* for hydrated carbonaceous chondrites, which have a lower limit of $Q_D^* > 1.4 \times 10^7$ erg/g.

We then use our Q_D^* estimate to determine the size-dependent impact strength, Y , of monolithic C-complex objects (see Eq. (M28)). The size dependence of strength is a consequence of the increase in the number and size of internal cracks and flaws with the size of an object. Strength measures a material’s ability to withstand a particular stress, such as compressive, tensile or shear [19]. An object’s response to an impact is dominated by one of these strengths. The formation of well-defined deep craters, as observed on Bennu’s boulders, is typically dominated by shear [19] or compressive strength [11]. In contrast, impacts onto brittle material lead to shallow spall craters formed by tensile failure. For impacts with $U = 5$ km/s and $\mu_G = 0.33 - 0.36$, a 1-m-diameter boulder on Bennu has $Y = 0.44 - 1.70$ MPa, which may approximate its shear strength and/or compressive strength. The lower range of these estimated values of Y are comparable to the tensile strength (inferred from high porosities) of boulders on Ryugu, which ranges from 0.2 to 0.28 MPa [20]. Our measured impact strength is lower than the 85 MPa compressive strength reported for the CM2 Sutter’s Mill meteorite [21], but similar to the 0.25–0.7 MPa compressive strength estimated for the ungrouped C2 Tagish Lake fireball [22].

Atmospheric detections of meteoroids are currently limited to objects of $> \sim 5$ cm in size [23]. The centimeter- to decimeter-scale near-Earth object (NEO) population is also measured by observations of impact flashes [24] and seismic events [25] on the Moon. For smaller impactor sizes, measurements are limited to objects with sizes that are less than a fraction of a millimeter,

the largest of which are derived from micro-crater counting on Apollo lunar samples [6]. Thus, there is a gap in our knowledge of the NEO size frequency distribution at the millimeter to centimeter scale, as objects of this size are too small to be detected by Earth-based observations and sufficiently large that they would have catastrophically disrupted rocks in the Apollo sample collection [26]. This gap also reflects our poor understanding of the transition between contributions from the cometary (smaller sizes) and asteroidal (larger sizes) sources to the NEO population [27]. We show below that Bennu’s meter-size boulders fill this gap by recording the history of impacts by millimeter- to centimeter-scale objects in near-Earth space.

In the higher-resolution image dataset, which resolves multiple craters on a given boulder, we measured 367 craters with diameters between 3 and 50 cm on 36 boulders with diameters 0.5 to 2.5 m. These boulders have a total surface area of 160 m². We fit a power-law curve to the cumulative size frequency distribution (CSFD) of the crater diameters that has a functional form of $N(> D_C) = A_0 D_C^\alpha$, where N is the cumulative number of craters greater than D_C normalized by the total collecting area, and A_0 and α are the fitting parameters. We find that the best fit has $\alpha = -2.69 \pm 0.07$ for a completeness limit of 13 cm (Fig. 4a). This value of α is consistent with that reported for larger near-Earth objects with diameters between 1 and 10 m, based on observations of fireballs and bolides [23]. Therefore, we postulate that these craters were created during Bennu’s residence time in near-Earth space. The knee in the CSFD at crater diameters less than 13 cm may be due to observational limitations or crater erasure through boulder surface refreshing [28], but it is unlikely to be due to changes in impact mechanics at that scale.

As the measured CSFD exponent is similar to that of NEOs [23], we assume that the average impact speeds are ~ 20 km/s [29]. Using our derived impact strength prescription for Bennu’s boulders, we find that $R_C/a = 20.1$. Thus, the impactor population that formed these impact craters ranges from ~ 1 mm to 2.5 cm. We find that the CSFD of the objects in this size range—a regime that has not previously been well characterized by models of the NEO population (Fig. 4b)—has a power-law distribution that differs from that of the micron to sub-millimeter population predicted by impacts onto orbiting spacecraft and Apollo-era observations of impact pits on lunar rocks [26]. Whereas the impact pits on lunar samples are thought to have been created from sub-mm meteoroids [26] likely originating from comets [30], we find that the NEO population of objects > 1 mm have an asteroidal origin, as Bennu’s boulders show that their CSFD has a larger exponent.

Extrapolating the derived fluxes from [23], we find that Bennu’s meter-scale boulders have been exposed to the NEO impactor population for 1.75 ± 0.75 Myr (Fig. 4b, Methods Section 5). This exposure age represents Bennu’s lifetime in near-Earth space since it dynamically and collisionally decoupled from the main asteroid belt. This derived age is within the limits of Bennu’s near-Earth lifetime predicted by dynamical calculations of NEA orbital evolution [31]. Other geophysical processes such as degradation via thermal fatigue or exfoliation, which is evident on Bennu [32], may lead to the exposure of fresh boulder faces. If the timescale for surface refreshing via these mechanisms is shorter than a few million years, then Bennu’s residence time in near-Earth space may be longer than the age we derived.

Our derived exposure age of Bennu’s meter-size boulders is substantially shorter than the expected total lifetime of this asteroid after catastrophic disruption of its parent [33]. As the source region

of NEAs is the main asteroid belt, Bennu has spent most of its lifetime in a collisional environment different than the one at its current orbit [2,32]. We use our disruption threshold of C-complex objects to assess the mean collisional lifetimes, τ_{coll} , of Bennu’s boulders in these distinct environments. For the main asteroid belt, we consider typical impact speeds ($U = 5$ km/s), observations of the asteroids’ size distribution, and models of their collisional evolution [2] to estimate $\tau_{coll} \sim 1$ Myr for a surface boulder with a 1-m radius (see Fig. 3b and Methods Section 4). This value is consistent with the young surface age derived from our analysis of the impact record on exposed boulder surfaces.

The near-Earth space environment has higher average impact speeds ($U = 20$ km/s) than the main belt [29]); however, the number density of potential disruptive impactors is far lower [2]. Combined with an increase in Q_D^* for higher impact speeds (compare the solid red line to the blue-shaded region in Fig. 3a), the relatively sparse impact environment in near-Earth space leads to the cessation of collisional disruption of meter-scale objects on the surface of asteroids: $\tau_{coll} = 57$ to 150 Myr, which is substantially greater than the mean dynamical lifetime of NEAs (<10 Myr) [31]. During Bennu’s residence time in the main belt, its surface boulders would have collisionally evolved more quickly. Once a C-complex asteroid dynamically and collisionally decouples from the main belt, impact cratering, rather than disruption, becomes the primary mechanism for impact-induced breakdown.

We conclude that the large craters on Bennu’s boulders ($R_C/R_T > 0.3$, for $R_T > 1$ m) were created by impacts with energies close to the disruption limit and formed during Bennu’s residence time in the main asteroid belt. Conversely, the small craters ($D_C < 50$ cm) observable on flat boulders were formed more recently, during Bennu’s residence time in near-Earth space over the past 1.75 ± 0.75 Myr.

References

1. Michel, P. et al. Collisions and Gravitational Reaccumulation: Forming Asteroid Families and Satellites. *Science* 294, 1696–1700 (2001).
2. Bottke, W.F., et al. Linking the collisional history of the main asteroid belt to its dynamical excitation and depletion. *Icarus* 19, 63–94 (2005).
3. Flynn, G.J., et al. Physical properties of the stone meteorites: Implications for the properties of their parent bodies. *Chemie der Erde* 78, 269–298 (2018).
4. Benz, W., and Asphaug, E. Catastrophic Disruptions Revisited. *Icarus* 142, 5–20 (1999).
5. Jutzi, M., et al. Fragment properties at the catastrophic disruption threshold: The effect of the parent body’s internal structure. *Icarus* 207, 54–65 (2010).
6. Grün, E. et al. Collisional balance of the meteoritic complex. *Icarus*, 62, 244–272 (1985).
7. Nakamura, A.M., et al. Impact process of boulders on the surface of asteroid 25143 Itokawa—fragments from collisional disruption. *Earth, Planets, and Space* 60, 7–12 (2008).

8. Golish, D.R., et al. Ground and In-Flight Calibration of the OSIRIS-REx Camera Suite. *Space Science Reviews* 216, Issue 1, 12 (2020).
9. DellaGiustina, D.N., et al. Overcoming the challenges associated with image-based mapping of small bodies in preparation for the OSIRIS-REx mission to (101955) Bennu. *Earth and Space Science* 5, 929–949 (2018).
10. Daly, M.G., et al. The OSIRIS-REx Laser Altimeter (OLA) Investigation and Instrument. *Space Science Reviews* 212, 899–924 (2017).
11. Murakami, Y., et al. Collisional disruption of highly porous targets in the strength regime: Effects of mixture. *Planetary & Space Science* 182, 104819 (2020).
12. Housen, K. Cumulative damage in strength-dominated collisions of rocky asteroids: Rubble piles and brick piles. *Planetary & Space Science* 57, 142–153 (2009)
13. Macke, R.J., Consolmagno, G.J., and Britt, D.T. Density, porosity, and magnetic susceptibility of carbonaceous chondrites. *Meteoritics & Planetary Science* 46, 1842–1862 (2011).
14. Holsapple, K.A., and Schmidt, R.M. Point source solutions and coupling parameters in cratering mechanics. *Journal of Geophysical Research* 92, 6350–6376 (1987).
15. Housen, K.R., and Holsapple, K.A. Ejecta from impact craters. *Icarus* 211, 856–875 (2011).
16. Nakamura, A.M. et al. Size dependence of the disruption threshold: laboratory examination of millimeter-centimeter porous targets. *Planetary and Space Science* 107, 45–52 (2015).
17. Sugita, S., et al. The geomorphology, color, and thermal properties of Ryugu: Implications for parent-body processes. *Science* 364, 252–252 (2019).
18. Yasui, M. Effects of oblique impacts on the impact strength of porous gypsum and glass spheres: Implications for the collisional disruption of planetesimals in thermal evolution. *Icarus* 335, 113414 (2020).
19. Holsapple, K.A. On the “strength” of the small bodies of the solar system: A review of strength theories and their implementation for analyses of impact disruptions. *Planetary & Space Science* 57, 127–141 (2009).
20. Grott, M., et al. Low thermal conductivity boulder with high porosity identified on C-type asteroid (162173) Ryugu. *Nature Astronomy* 3, 971–976 (2019).
21. Jenniskens, P. et al. Radar-Enabled Recovery of the Sutter’s Mill Meteorite, a Carbonaceous Chondrite Regolith Breccia. *Science* 338, 1583–1587 (2012).

22. Brown, P.G. et al. An entry model for the Tagish Lake fireball using seismic, satellite and infrasound records. *Meteoritics & Planetary Science* 37, 661–675 (2002).
23. Brown, P. et al. The flux of small near-Earth objects colliding with the Earth. *Nature* 420, 294–296 (2002).
24. Avdellidou, C., and Vaubaillon, J. Temperatures of lunar impact flashes: mass and size distribution of small impactors hitting the Moon. *Monthly Notices of the Royal Astronomical Society* 484, 5212–5222 (2019).
25. Kawamura, T. et al. Cratering asymmetry on the Moon: New insight from the Apollo Passive Seismic Experiment. *Geophysical Research Letters* 38, 15201 (2011).
26. Hörz, F., et al. Catastrophic Rupture of Lunar Rocks: A Monte Carlo Simulation. *The Moon*. 235–258 (1975).
27. Pokorny, P., and Brown, P. G. A reproducible method to determine the meteoroid mass index. *Astronomy & Astrophysics* 592, A150 (2016).
28. Delbo, M., et al. Thermal fatigue as the origin of regolith on small asteroids. *Nature* 508, 233–236 (2014).
29. Moorhead, A. V. Deconvoluting measurement uncertainty from the meteor speed distribution. *Meteoritics & Planetary Science* 53, 1292–1298 (2018).
30. Nesvorný, D. et al. Cometary Origin of the Zodiacal Cloud and Carbonaceous Micrometeorites. Implications for Hot Debris Disks. *The Astrophysical Journal* 713, 816–836 (2010).
31. Michel, P., and Delbo, M. Orbital and thermal evolutions of four potential targets for a sample return space mission to a primitive near-Earth asteroid. *Icarus* 209, 520–534 (2010).
32. Molaro, J. L., et al. In situ evidence of thermally induced rock breakdown widespread on Bennu’s surface. *Nature Communications* 11, 2913 (2020).
33. Walsh, K.J., et al. Craters, boulders and regolith of (101955) Bennu indicative of an old and dynamic surface. *Nature Geoscience* 12, 242–246 (2019).

Figure 1 | Craters are observed on Bennu’s boulders in images and laser altimetry data. The left columns show examples of PolyCam images of craters on boulders, and the right columns show the corresponding topographical detail from OLA point cloud data. The largest craters on each boulder are highlighted by dashed circles. **a**, A boulder approximately 2 m in diameter with a flat exposed face with multiple centimeter-scale impact craters, located at 35.4° S and 316.2° E. **b**, A boulder approximately 5 m in diameter with multiple ~ 0.5-m impact craters, located at 9.6°

N and 16.2° E. **c**, A boulder approximately 17 m in diameter with a ~ 5-m impact crater, located at 0.49° S and 81.7° E. **d to f**, OLA point cloud of the boulders shown in **a to c**, respectively.

Figure 2 | The maximum crater size on a boulder depends on boulder strength. A global search using the Bennu basemap revealed 258 boulders with craters larger than 0.3 m. **a**, For each boulder with craters, the radius of the boulder (R_T) and its largest crater (R_C) were measured. By building up a large database of these measurements (black circles), we determine the maximum crater size $R_{C,max}$ (highlighted by the dashed red box; Boulders 1 to 7 in Supplementary Information Table 1) for a given boulder size. Error bars are based on the estimated uncertainty in the measurement of the sizes of craters and boulders, ~ 15 cm. **b**, The dimensions of the boulders and craters that have $R_C = R_{C,max}$ are re-measured using OLA data (red triangles and yellow squares; Methods Section 3) to obtain better confidence intervals. The uncertainty in the OLA-measured crater diameter is the 1-sigma standard deviation in the crater rim fit. We find that only five of the seven boulders (Boulders 1 to 5) are close to the disruption limit (red triangles). We fit a straight line through the red triangles ($r^2 = 0.84$) to determine $\mu_S = 0.47 \pm 0.07$. The uncertainty in μ_S is based on the estimated uncertainty in the OLA-measured crater diameters and the boulder diameters (see Methods). **c** The OLA profile of Boulder 5 (the same boulder as shown in Fig. 1c), showing its largest crater. The boulder has a circle-equivalent diameter of 14 m. The crater has an OLA-measured diameter of 4.77 ± 0.41 m. The profiles of Boulders 1 to 4 are shown in ED Figure 1.

Figure 3 | Bennu’s boulders are relatively weak and have short lifetimes in the main asteroid belt. **a**, Using size measurements of craters on Bennu’s boulders, we derived their catastrophic disruption threshold for impact speeds of 5 km/s (blue-shaded region, with variation driven by uncertainty in value of $\mu_G \in [0.33, 0.36]$) and 20 km/s (red solid line, $\mu_G = 0.345$). We compare this threshold to those of basalt (black dotted line) and pumice (black dashed line) derived from numerical simulations of impacts at angles of 45° [16,17]. **b**, Bennu’s boulders are weaker than porous pumice (black dotted line) and non-porous basalt targets (black dashed line) of the same size. The main belt asteroid (MBA) mean collisional lifetime (blue-shaded region) of 1-m-diameter C-complex objects is ~1 to 3 Myr, whereas a NEO of the same size and composition has a collisional lifetime (red-shaded region) of ~57 to 150 Myr, longer than the expected dynamical lifetime.

Figure 4 | The surface exposure age of Bennu’s meter-size boulders is ~ 1.75 Myr. **a**, The CSFD of impact features on Bennu’s meter-size boulders, normalized by surface area. The measured CSFD exponent is similar to that measured from observations of bolides and fireballs [23]. The error bars are the standard error of the mean, with a sample size set by the cumulative number for each data point. **b**, For $\mu_G = 0.345$, Bennu’s meter-size boulder population gives a surface age of 1.75 Myr, which is likely equivalent to Bennu’s lifetime in near-Earth space, t_{NEA} . We compare this to a 7-Myr exposure age calculated by using the sub-millimeter NEO impactor flux [6], which has a steeper slope that only matches the largest few craters we observe. The ranges of sizes detected by lunar impact flash monitoring [24] and Apollo seismic data [25] are also shown. **c-f**, Examples of boulders used in the analysis in panel (a); the full list of boulders is presented in ED Table 2. **c**, A boulder approximately 2 m in diameter, located at 4.5° S and 262.8° E. **d**, A cratered boulder approximately 1.7 m in diameter, located at 5.2° N and 271.5° E. **e**, A cratered

boulder approximately 1.7 m in diameter, located at 8° S and 283.2° E. **f**, A cratered boulder approximately 1.1 m in diameter, located at 12.5° S and 280.7° E.

Acknowledgements

We thank D.P. Hamilton, K.A. Holsapple, and P. Pravec for helpful insights and feedback. This material is based upon work supported by NASA under Contract NNM10AA11C issued through the New Frontiers Program. We are grateful to the entire OSIRIS-REx Team for making the encounter with Bennu possible. M.D., C.A., and P.M. would like to acknowledge the French space agency CNES. C.A. and M.D. acknowledge support from the ANR “ORIGINS” (ANR-18-CE31-0014). C.A. was supported by the French National Research Agency under the project “Investissements d’Avenir” UCAJEDI ANR-15-IDEX-01.

Author contributions

R.-L.B. led the conceptualization of the study, the images and OLA data analysis, construction of the analytical formalism to measure boulder impact strength from crater sizes, the interpretation of results, and manuscript preparation efforts. K.J.W. contributed to the conceptualization of the study, the interpretation of results, and manuscript preparation efforts. O.S.B. created OLA DTMs of boulders, measured crater dimensions with these products, contributed to the interpretation of results, and the preparation of the manuscript. D.N.D., E.R.J., and C.A.B. provided GIS guidance and expertise, contributed to the image analysis, interpretation of the results, and the preparation of the manuscript. M.M.A., M.G.D., and R.T.D. contributed to the OLA data analysis, interpretation of the results, and the preparation of the manuscript. W.F.B., P.M., C.A., M.D., J.L.M., E.A., E.B.B., M.C.N., M.P., H.C.C. Jr., S.R.S., D.T., and C.W.V.W. contributed to the interpretation of the results and the preparation of the manuscript. B.R. and D.R.G. processed the PolyCam images presented in the manuscript. D.S.L. leads the mission and contributed to analysis and writing.

METHODS

1. Deriving boulder strength against cratering and catastrophic disruption from observations of the maximum crater sizes

The failure mechanics of monolithic C-complex asteroids are poorly understood because their meteoritic counterparts (CM and CI meteorites) are relatively rare and generally small; therefore, destructive testing of samples to determine their strength against impacts is infeasible [34]. Our current best understanding of the impact strength of monolithic C-complex asteroids comes from experiments that use terrestrial analogs [35] such as pumice [36] or asteroid regolith simulants [37]. Insights have also been gained from experiments into weak solid targets such as sandstones [38]. The results of these impact experiments into centimeter-scale targets are then used to calibrate numerical simulations of impact outcomes at planetary scales [4,5] and the collisional evolution of the early Solar System [2]. Here, we show how we developed a novel framework to estimate the disruption threshold and impact strength of C-complex monolithic objects by combining scaling laws for cratering and catastrophic disruption with observations of craters on Bennu's boulders. This type of analysis has been previously applied to the study of the largest craters on planetary bodies greater than tens of kilometers in diameter by using scaling laws [39]. Here, we extend it to objects of arbitrary size.

1.1 Catastrophic Disruption Equations

The catastrophic disruption threshold defines the specific impact energy where a target body will lose half its mass. There are two regimes for catastrophic disruption: a strength regime and a gravity regime [4, 14]. The strength regime typically dominates for small objects up to a few hundred meters, whereas the gravity regime dominates for larger objects. In the strength regime, the specific energy required for catastrophic disruption, Q_S^* , decreases with the target's size, R_T :

$$Q_S^* \propto R_T^{9\mu_S/(3-2\phi)} U^{2-3\mu_S} \quad (M1)$$

where μ_S and ϕ are dimensionless material constants [39].

ϕ is a measure of the strain-rate dependence of the material strength. The value of ϕ ranges from 6 to 12, depending on a material's size distribution of flaws and the loading rate [40]. Ref. [40] found that measurements of ϕ through static strength tests ($\phi \sim 12$) differ from those derived from dynamic collision experiments ($\phi \sim 6$). Here, we adopt $\phi = 6$ when analyzing the catastrophic disruption threshold of boulders, giving

$$Q_S^* \propto R_T^{-\mu_S} U^{2-3\mu_S} \quad (M2)$$

where μ_S is a measure of how energy and momentum from the projectile are coupled to the target and is constrained to fall between 1/3 for pure momentum scaling and 2/3 for pure energy scaling [14]. As we will show in Section 1.3, the value of μ_S for Bennu's boulders can be estimated through measurements of craters on their surface. In the gravity regime, the specific impact energy, Q_G^* , increases with target size, as the body's self-gravity starts to become sufficient for re-accumulation,

$$Q_G^* \propto R_T^{3\mu_G} U^{2-3\mu_G} \quad (M3)$$

where μ_G describes the mass and velocity coupling of the impactor to the target in the gravity regime. We adopt separate values of the material constant μ for the two different regimes. Although this is not classically done for cratering equations, we introduce this formalism here to distinguish between the orders of magnitude variation in the cratering and disruption size scales that we are concerned with in this study. Though not explicitly explored, numerical simulations of catastrophic disruption show that the value of μ indeed changes with size scale [4,5]

The total specific impact energy required for catastrophic disruption, Q_D^* , is the sum of the strength and gravitational terms, Eqs. (M2) & (M3), which can be written as:

$$Q_D^* = q_S R_T^{-\mu_S} U^{2-3\mu_S} + q_G R_T^{3\mu_G} U^{2-3\mu_G} \quad (M4)$$

Therefore, to obtain Q_D^* for C-complex objects, we need to determine the values of the catastrophic disruption parameters q_S , q_G , μ_S , and μ_G . The material constants q_S and q_G set the scale of the catastrophic disruption threshold in the strength and gravity regimes, respectively. The material constants μ_S and μ_G set the size and velocity dependence of the catastrophic disruption threshold.

1.2 Cratering Equations

Ref. [41] introduced the idea that point source phenomena have a single scalar measure of magnitude (termed the coupling parameter, C), and that C is the product of the impactor radius, a , its velocity, U , and its mass density, δ ,

$$C = aU^\mu \delta^\nu \quad (M5)$$

where μ and ν are material constants. Ref [14] expanded that theory to generalized formulations of crater properties based on the Buckingham π theorem, with the crater volume, V_C , given by:

$$V_C = f[aU^\mu \delta^\nu, \rho, Y, g] \quad (M6)$$

where ρ and Y are the density and strength of the target, respectively, g is the surface gravity, and the π group parameters are related by

$$\pi_V = K_1 [\pi_2 \pi_4^{-1/3} + (K_2 \pi_3)^{(2+\mu)/2}]^{-3\mu/(2+\mu)} \quad (M7)$$

and

$$\pi_V = \frac{\rho V_C}{m_i} = \frac{\rho (R_C/K_r)^3}{m_i} \quad (M8)$$

where $m_i = (4/3)\pi a^3$ is the projectile mass. K_1 , K_2 , and K_r are crater scaling constants that depend on the target material. K_r relates the radius of the crater to its volume. Based on our

observation of d/D ratios of ~ 0.2 for craters on boulders, we set $K_r = 1.2$. Based on impact experiments with solid targets, Ref. [42] find that $K_1 = 0.2$ and $K_2 = 1$. The π -group parameters that control the cratering efficiency, π_V , are

$$\pi_2 = \frac{ga}{U^2} \quad (M9)$$

$$\pi_3 = \frac{Y}{\rho U^2} \quad (M10)$$

$$\pi_4 = \frac{\rho}{\delta} \quad (M11)$$

The impact strength of the target, Y , has a size dependence, as larger objects will have larger internal flaws [40]. The size-dependent impact strength in the cratering regime can be written as,

$$Y = Y_0 R_T^{-1/n} \quad (M12)$$

where $n = 4$ for normal craters dominated by shear strength, and $n = 2$ for spall craters. Y_0 is the impact strength of a target with a radius of 1 cm. As we see little evidence for spall-dominated craters on Bennu's boulders, we adopt a value of $n = 4$ [43,40].

1.3 Transition from Cratering to Catastrophic Disruption

For spacecraft observations, crater sizes are measured, but impactor properties are largely unknown. Namely, the impactor radius, a , derived from a crater radius, R_C , is a function of the impactor properties (δ and U) and target properties (ρ , Y). Here, we use observations of the maximum ratio of crater size to boulder size, R_C/R_T , to derive the mechanical properties of the boulders by assuming that these impacts represent the maximum allowable specific energies for cratering before the onset of catastrophic disruption.

Such a theoretical framework was first used by [39] to predict the maximum crater radius on a planetary body and was later revised by [44], who used spacecraft observations of craters on asteroids and moons to craft a Q_D^* law in the gravity regime.

Given the crater sizes from the observational data, R_C , we derive the impactor size, a required to (i) form a crater in the strength regime, (ii) form a crater in the gravity regime, (iii) disrupt a body in the strength regime, and (iv) disrupt a body in the gravity regime.

For cratering in the strength regime, this is done by setting:

$$\pi_V = K_1 (K_2 \pi_3)^{-3\mu_S/2} \quad (M13)$$

For cratering in the gravity regime:

$$\pi_V = K_1 \pi_2^{-3\mu_G/(2+\mu_G)} \pi_4^{\mu_G/(2+\mu_G)} \quad (M14)$$

Here, as for the disruption equations, we introduce separate values of the material constant μ for the different cratering regimes.

For disruption in the strength regime:

$$Q_S^* = \frac{1}{2} \frac{\delta a^3 U^2}{\rho R_T^3} = q_S R_T^{-\mu_S} U^{2-3\mu_S} \quad (M15)$$

For disruption in the gravity regime:

$$Q_G^* = \frac{1}{2} \frac{\delta a^3 U^2}{\rho R_T^3} = q_G R_T^{3\mu_G} U^{2-3\mu_G} \quad (M16)$$

Solving each of the previous Eqs.(M13-M16) for a , we find for

(i) strength-regime cratering

$$a = (4\pi/3)^{-1/3} \left(\frac{K_2^{\mu_S/2}}{K_r K_1^{1/3}} \right) Y^{\mu_S/2} U^{-\mu_S} \rho^{\frac{1-\mu_S}{3}} \delta^{-1/3} R_C \quad (M17)$$

(ii) gravity-regime cratering

$$a = (K_1^{1/3} K_r)^{-(2+\mu_G)/2} (G)^{\mu_G/2} (4\pi/3)^{\frac{\mu_G-1}{3}} \rho^{\frac{2+5\mu_G}{6}} \delta^{-\frac{(1+\mu_G)}{3}} R_C^{\frac{2+\mu_G}{2}} R_T^{\mu_G/2} U^{-\mu_G} \quad (M18)$$

(iii) strength-regime disruption

$$a = (2q_S)^{1/3} R_T^{\frac{-\mu_S}{3}+1} U^{-\mu_S} (\rho/\delta)^{1/3} \quad (M19)$$

and (iv) gravity-regime disruption

$$a = (2q_G)^{1/3} R_T^{\mu_G+1} U^{-\mu_G} (\rho/\delta)^{1/3} \quad (M20)$$

Then, the ratio of maximum crater size to target size, $R_{C,\max}/R_T$, can be solved for impacts in the different regimes.

For the strength regime, this is done by equating Eqs. (M17) and (M19), and including the size-dependence of Y (Eq. M12), giving:

$$\frac{R_{C,\max}}{R_T} = \left(\frac{8\pi}{3} q_S \right)^{1/3} \left(\frac{K_r K_1^{1/3}}{K_2^{\mu_S/2}} \right) (\rho/Y_0)^{\mu_S/2} R_T^{-5\mu_S/24} \quad (M21)$$

In the strength regime, the maximum crater size has a negative correlation with size of the boulder to the power of $-5\mu_S/24$. Therefore, we are able to measure the value of μ_S for Bennu's boulders by measuring the slope of a plot of $\log(R_{C,\max}/R_T)$ to $\log(R_T)$. Furthermore, the intercept of that curve will provide the value of Y_0 once q_S is calculated. Laboratory impact experiments have

shown that cratering efficiency may increase when the size of the crater becomes comparable to the target boulder size [45]; however, this is thought to be due to spallation, which is not a dominant mechanism for the craters we observe on Bennu’s surface.

For the gravity regime, this is done by equating Eqs. (M18) and (M20), giving:

$$\frac{R_{C,\max}}{R_T} = K_1^{1/3} K_r (2q_G)^{\frac{2}{3(2+\mu_G)}} G^{\frac{-\mu_G}{2+\mu_G}} (4\pi/3)^{\frac{2(1-\mu_G)}{3(2+\mu_G)}} \rho^{\frac{-5\mu_G}{3(2+\mu_G)}} \delta^{\frac{2\mu_G}{3(2+\mu_G)}} \quad (M22)$$

In the gravity regime, the value of $R_{C,\max}/R_T$ is constant. For impacts into asteroids with known density ρ , by impactors with assumed density δ , the value of q_G can be calculated if $R_{C,\max}/R_T$ and μ_G are known, by manipulating the previous equation to give:

$$q_G = \frac{1}{2} G^{3\mu_G/2} (K_1^{1/3} K_r)^{3(2+\mu_G)/2} (4\pi/3)^{\mu_G-1} \rho^{5\mu_G/2} \delta^{-\mu_G} \left(\frac{R_{C,\max}}{R_T} \right)^{3(2+\mu_G)/2} \quad (M23)$$

Finally, we note an intermediate regime, where strength-regime cratering leads to disruption that depends on both the strength and gravity regime components. This regime must exist for rubble-pile objects such as Bennu and Ryugu, whose gravity is sufficiently low that cratering occurs in the strength regime, but which are sufficiently large such that gravitational re-accumulation is an important factor in their resistance against catastrophic disruption. These are transitional objects that lie above the minimum of the Q_D^* curve, which has a corresponding target radius $R_T = R_w$, the “weakest” object of that material type. The value of R_w can be derived by finding the radius for which $dQ_D^*/dR_T = 0$. From Eq. (M4), and setting $a \equiv -3\mu_S/5$ and $b \equiv 3\mu_G$,

$$\begin{aligned} Q_D^* &= (q_S R_T^a U^{3a+b} + q_G R_T^b) U^{2-b} \\ \frac{dQ_D^*}{dR_T} &= (q_S a R_T^{a-1} U^{3a+b} + q_G b R_T^{b-1}) U^{2-b} \end{aligned} \quad (M24)$$

Setting $R_T = R_w$, and solving for R_w by setting $dQ_D^*/dR_T = 0$,

$$R_w = \left(\frac{-b q_G}{a q_S U^{3a+b}} \right)^{\frac{1}{a-b}} \quad (M25)$$

Because R_w can be estimated from observations of monolithic C-complex boulders, we can rearrange this equation to obtain the final unknown parameter in Eq. (M4), q_S :

$$\begin{aligned} q_S &= \frac{-b q_G R_w^{b-a}}{a U^{3a+b}} \\ &= \frac{3\mu_G q_G R_w^{3\mu_G+\mu_S}}{\mu_S U^{3(\mu_G-\mu_S)}} \end{aligned} \quad (M26)$$

Unlike previous derivations of Q_D^* with scaling laws [44], having different values of the coupling parameter μ for the strength regime and gravity regime leads to a velocity dependence of the q_S as found in numerical simulations [4,5].

Finally, we solve Eq. (M4) for a and equate that to Eq. (M17) to derive the following prescription for $R_{C,\max}/R_T$ in the intermediate regime:

$$\frac{R_{C,\max}}{R_T} = (8\pi/3)^{1/3} \left(\frac{K_r K_1^{1/3}}{K_2^{\mu/2}} \right) (\rho/Y)^{\mu_S/2} (q_S R_T^{-\mu_S} + q_G R_T^{3\mu_G} U^{3(\mu_S - \mu_G)})^{1/3}. \quad (M27)$$

In the intermediate regime, the value of $R_{C,\max}/R_T$ is a complicated function of μ_G , μ_S , q_G , and q_S . Therefore, although a value of μ_G cannot be explicitly derived, we provide this prescription for completeness. We use literature values of μ_G from numerical simulations of catastrophic disruption in the gravity regime [46]. Therefore, by using Eqs. (M20), (M21), and (M25), we can derive the Q_D^* law for monolithic C-complex objects. This is explicitly described in the following three steps.

Step 1. Measuring μ_S from observations of Bennu's boulders

In this step, we determine the strength-regime size dependence of the disruption threshold. The value of μ_S is determined using Eq. (M21) by observing that $R_{C,\max}/R_T \propto R_T^{-5\mu_S/24}$ in the strength regime. As shown in main text, we complete this step by fitting the curve of maximum crater radii (Fig. 2).

For Bennu's boulders that have visible craters, we measured the largest craters on each boulder in the basemap dataset (Fig. 2, Supplementary Information Table 1). We isolated craters that have $R_C \sim R_{C,\max}$ by the following means: (i) measuring the crater size to host-boulder size, and (ii) down-selecting to the subset of craters that have an R_C/R_T within 0.1 of the global maximum value (measurements within dashed red box Fig. 2a). The boulder and crater dimensions of this subset were then measured using OLA data for better confidence in the measured values, and only craters that are truly the largest for a given host-boulder size are determined to have $R_C = R_{C,\max}$ (red triangles in Fig. 2b). By comparing the values of $R_{C,\max}/R_T$ to R_T , we calculated the value of $\mu_S = 0.47$ by finding the best-fit slope. This value of μ_S is slightly larger than that determined from laboratory impact experiments into porous targets [15].

Step 2. Using literature values of μ_G and gravity regime $R_{C,\max}/R_T$ to calculate q_G

In this step, we derive the gravity-regime disruption scale and size dependence from classical scaling laws and the results of numerical simulations described in the literature. Ref. [46] compiled data from catastrophic disruption simulation from various sources and found that across (i) a variety of target compositions, (ii) five orders of magnitude in size (~ 0.4 to 4×10^5 km), and (iii) nine orders of magnitude in impact energy, the value of μ_G lies between a narrow range of 0.33 and 0.36 for the bodies with sizes < 1000 km.

Furthermore, the prescription given by Eq. (M27) suggests that $R_{C,\max}/R_T$ increases with R_T until reaching a maximum constant value after the transition from strength- to gravity-scaled cratering (since $R_{C,\max}/R_T$ is independent of R_T in the gravity regime as shown in Eq (M28)). We propose that this growth in $R_{C,\max}/R_T$ leads to a maximum value set by the transition point between strength- and gravity-scaled cratering. In the gravity regime, $R_{C,\max}/R_T \sim 1.0$ for rocky bodies [47,48]. The value of μ_G is the largest uncertainty in our analysis; therefore, we evaluate the range of calculated values for $\mu_G \in [0.33,0.36]$. We can then use Eq. (M23) to calculate q_G .

Step 3. Calculating q_S using observations of the largest monolithic C-complex object

In the last step, we establish the scale of strength-regime disruption by noting that the two regimes, strength and gravity, intersect at the size of the largest observed monolithic C-complex object, which corresponds to the size of the weakest C-complex object, R_w . R_w also represents the transition between monolithic and rubble-pile asteroids, gravitational aggregates of solid material which have substantial internal porosity [49]. From scaling laws, ref. [44] gives $R_w = 3$ km, whereas numerical simulations give $R_w = 100$ to 400 m [4]. The largest monolithic C-complex object observed to date is the boulder Otohime on Ryugu, which has a diameter of 160 m [17]. Therefore, we adopt a value of $R_w = 80$ m. We use Eq. (M26) to calculate q_S .

1.4 The cratering efficiency of C-complex objects

As noted in the derivation of Eq. (M21), the value of the cratering strength, Y , can be measured once the value of q_S is known by using the curve-fitting results presented in the main text (Fig. 2), by noting that the intercept, I , of the $\log(R_{C,\max}/R_T)$ to $\log(R_T)$ plot, is given by:

$$I = \left(\frac{8\pi}{3} q_S\right)^{1/3} \left(\frac{K_r K_1^{1/3}}{K_2^{\mu_S/2}}\right) (\rho/Y_0)^{\mu_S/2} \quad (M28)$$

We can then use these values of Y in Eq. (M17) to determine the value of the crater-to-impactor size ratio, R_C/a . Combined with an understanding of the impactor population, the value of R_C/a can then provide a surface for strength-dominated impacts on to C-complex objects. For impacts with $U = 5$ km/s and $\mu_G = 0.33$ to 0.36, $Y_0 = 2$ to 8 MPa. For a 1-m diameter boulder, $Y = 0.44$ to 1.70 MPa and $R_C/a = 14.4$ to 19.8.

2. Mapping craters on boulders

2.1 Mapping of largest craters on individual boulders using lower-resolution images

Measurements of the largest craters found on boulders were made by projecting the Bennu basemap [50] onto the v28 80-cm-resolution Bennu shape model (an update to the shape model presented in ref. [51]) using the Small Body Mapping Tool (SBMT [52]). The basemap was created from images taken by the PolyCam instrument during the Detailed Survey phase of the OSIRIS-REx mission [53] and has a ground sample distance of about 5.25 cm/pixel [9]. Boulders were mapped using ellipses to obtain their approximate areal extent, and craters were mapped using circles to measure their longest axis. Here, we report the circular-area equivalent boulder radius, R_T , such that for a measured area of a boulder, A_B , $R_T = \sqrt{A_B/\pi}$. In total, we found 258 boulders with at least one surface crater. The largest crater on each of these boulders was measured and cataloged. The range of host boulder sizes is 1.45 to 50 m, and the range of crater diameters is 0.3 to 5 m. Craters were identified by morphologic characteristics including circular depressions and raised rims. Craters were distinguished from depressions in boulders formed via processes other than impact cratering by their relatively symmetric appearance and their large size. The only other process that we identified that can produce circular pits on rock faces is vesicle formation, which form on igneous rocks that are absent on the surface of Bennu. Furthermore, the diameters of vesicles are smaller than 1 mm.

2.2 Mapping centimeter- to decimeter-scale craters on boulders using higher-resolution images

Craters on the scale of centimeters to decimeters were identified on boulders using the same methodology described above to distinguish impact craters from non-impact features in PolyCam images taken during the Orbital A and B phases of the OSIRIS-REx mission [9]. These PolyCam images had pixel scales ranging from 1 to 2.5 cm. Orbital data are acquired near the terminator and have phase angles $> 90^\circ$ in some instances, which allowed us to identify shallow mini-craters on boulders with flat faces. Using the geographic information system software ArcMap, boulder faces were mapped with polygons, and craters overlaying these faces were mapped with circles. ArcMap was used for this task as it allowed for a more precise measurement of the area of polygonal boulder faces than SBMT. The flat boulder faces have a total surface area of 160 m². Images were projected onto the v28 80-cm-resolution shape model of Bennu using two-point equidistant projections centered on a boulder's coordinates.

3. Measuring crater dimensions using laser altimetry data

During the Orbital B Global Mapping subphase [9], the OSIRIS-REx spacecraft was in a near-terminator orbit at an average range of about 700 m from the surface of Bennu. OLA collected 892 overlapping scans of the surface, each containing 3.3 million measurements. A global point cloud dataset was assembled using techniques previously described in [54, 55]. The resulting point cloud has ground sample distances and ranging resolution of ~ 5 cm globally.

To measure the depth and diameters of craters on boulders, we extracted point clouds in regions centered on boulders that have the largest craters for their given size, mapped in the global mosaic (as described in Methods Section 2.1). Individual digital terrain models (DTMs) of these boulders were then created. The properties of the craters on the boulders were then measured by:

1. Mapping out the location of the crater rim using a rendered image of the topography and the high-resolution contours as a guide.
2. Fitting an ellipse to the crater rim and using the mean of the ellipse dimensions to estimate a diameter and compute an estimate of the standard deviation.
3. Fitting a plane to the mapped rim, and using this plane and the diameter, computed in step 2, to measure the crater diameter-depth from the height above the plane.
4. Estimating the uncertainty by using two rim fits: one for the 90% best fit rims height, and one for the entire rim heights, giving a more representative error.
5. Displaying contours on a DTM visualization and hand-picking the depth as the reasonable lowest point in the crater This is done by hand as numerical procedures may sometimes select a crater within a crater or a crack between two rocks that is not representative of the actual lowest point in the crater.

We also measured crater dimensions through the use of crater profiles by:

6. Constructing eight profiles across the hand-picked crater center.
7. Verifying the automatically detected crater rims.
8. Selecting several representative profiles to compute a profile-based diameter This hand-picking step is necessary to avoid the inclusion of large rocks at the edge of crater that might lead to a miscalculation of the true rim height.
9. Determining depth for the profiles using the same procedure as step 5.

Here, we report on the crater dimensions derived from the profile-based measurements, as they provide tighter constraints on the computed value of μ_S (see Methods Section 1.3). Examples of these profiles are shown in ED Figure 1.

4. Boulder mean collisional lifetime calculation

The mean collisional lifetime of a boulder of a given diameter, D_B , on the surface of Bennu is calculated by determining the impact rate of projectiles with diameters, D_{imp} , that provide the necessary specific impact energy required for catastrophic disruption of the target boulder. In the main asteroid belt, this is done by assuming a constant impact probability, $P_i = 2.9 \times 10^{-18} \text{ km}^{-2} \text{ yr}^{-1}$, for the collision of MBAs and a mean impact speed, $\langle v_{\text{imp}} \rangle = 5.3 \text{ km/s}$ [2]. D_{imp} is then determined using our derived value of Q_D^* for $U = \langle v_{\text{imp}} \rangle$.

To determine the total population of potential disruptive colliders, we first consider the CSFD, $N_{C, \text{MBA}}$, of MBAs calculated from observations of the MBA size distribution and models of their collisional evolution [2]. By numerically differentiating $N_{C, \text{MBA}}$, we derive the incremental size frequency distribution $N_{I, \text{MBA}}$ of MBAs with diameters D :

$$N_{I, \text{MBA}}(D_k) = N_{C, \text{MBA}}(\geq D_k) - N_{C, \text{MBA}}(\geq D_{k+1}) \quad (\text{M29})$$

where k is the index of the logarithmically binned CSFD data and $D_{\text{imp}, k+1} > D_{\text{imp}, k}$. Then, the number of disruptive impacts, N_{MBA} , over a mean time interval, t_{coll} , of a surface boulder with diameter, D_B , by an object with diameter D_{imp} is given by:

$$N_{\text{MBA}} = N_{I, \text{MBA}}(D_{\text{imp}}) \times P_i \times \frac{1}{2} \left(\frac{D_{\text{imp}}}{2} + \frac{D_B}{2} \right)^2 \times t_{\text{coll}} \quad (\text{M30})$$

where the third term on the right side of Eq. (M30) is the collisional cross-section divided by 2, as we approximate that a boulder resting on the surface of an asteroid is shielded from half of all potential impactors. The mean collisional lifetime is then calculated by setting $N_{\text{MBA}} = 1$ and solving for t_{coll} .

In near-Earth space, we perform a similar analysis by using the cumulative impact flux determined by ref. [24] based on observations of bolide detonations in Earth's atmosphere. The cumulative number of objects with diameters greater than D colliding with Earth per year is given by Eq. (3) in ref. [24]. We normalize this cumulative flux to the cross-sectional area of a surface boulder with diameter D_B to obtain:

$$N_{C, \text{NEA}}(D) = 10^{1.568} D^{-2.7} \times \frac{(D_B/2)^2}{R_{\text{Earth}}^2} \quad (\text{M31})$$

where R_{Earth} is Earth's radius. Then, the number of disruptive impacts in near-Earth space, N_{NEA} , over t_{coll} is determined by numerically integrating Eq. (M31) to find:

$$N_{\text{NEA}} = N_{I, \text{NEA}}(D_{\text{imp}}) \times t_{\text{coll}} \quad (\text{M32})$$

The mean collisional lifetime in near-Earth space is then calculated by setting $N_{\text{NEA}} = 1$, and solving for t_{coll} .

5. Exposure age of meter-sized boulders with multiple impact features

The surface exposure age of meter-sized boulders was determined by comparing the cumulative number of craters between 3 and 50 cm measured in Orbital A and B images (Methods Section 2.2). We measured 367 craters on 36 boulders with exposed faces that have a total area of 160 m² (ED Table 2). We fit a power-law curve to the CSFD of the crater diameters that has a functional form of $N(> D_c) = A_0 D_c^\alpha$, where N is the cumulative number of craters greater than D normalized by the total collecting area, and A_0 and α are the fitting parameters. We find that the best fit has $\alpha = -2.69 \pm 0.07$ for a completeness limit $C = 13$ cm.

We calculated the surface age by using the ref. [24] impact flux described in the previous section, as their CSFD slope ($\alpha = -2.7$) matches our observations. We compare this to the NEO flux obtain by ref. [6] (see their Eq. (A3)), which has a steeper slope ($\alpha \sim -4$), that is only matched by the largest five craters in our orbital dataset of craters on meter-sized boulders.

Uncertainty Estimate for μ_s

We calculate an estimate of the uncertainty in μ_s through error propagation analysis.

For the functional form: $y = x^w$, where y , x , and w are uncorrelated variables with associated uncertainties, then the standard uncertainty can be expressed as [56]:

$$(u(y)/y)^2 = w^2((u(x)/x)^2 + (\ln x)^2(u(w)/w)^2) \quad (M33)$$

where $u(y)$, $u(x)$, and $u(w)$ are the uncertainties in y , x , and w , respectively. As we are trying to estimate the uncertainty in the exponent of this function form, we rearrange the equation:

$$u(w) = (1/\ln(x))((u(y)/y)^2 - w^2(u(x)/x)^2)^{1/2} \quad (M34)$$

For our purposes, $y = R_{c,max}/R_t$, $x = R_t$, and $w = -5\mu_s/24$.

The uncertainty in $R_{c,max}/R_t$, $u(R_{c,max}/R_t)$, is given by:

$$u(R_{c,max}/R_t) = R_{c,max}/R_t \left((u(R_c)/R_c)^2 + (u(R_t)/R_t)^2 \right)^{1/2} \quad (M35)$$

where $u(R_c)$ and $u(R_t)$ is the uncertainty in R_c and R_t , respectively. $u(R_c)$ is driven by uncertainty in the location of the crater rim. The values of $u(R_c)$ are given in ED Table 1. We consider $u(R_t) \sim 15$ cm, equivalent to ~ 3 pixels in the high-resolution image data.

The uncertainty in μ_s , $u(\mu_s)$, is given by:

$$u(\mu_s)^2 = u(w)^2(-24/5)^2 \quad (M36)$$

Finally, giving:

$$u(\mu_s) = (24/5)(1/\ln(R_t)) \left(\left(u(R_{c,max}/R_t)/(R_{c,max}/R_t) \right)^2 - w^2(u(R_t)/R_t)^2 \right)^{1/2} \quad (M37)$$

Taking mean values for R_t , $(R_{c,max}/R_t)$, and $u(R_{c,max}/R_t)$, we find $u(\mu_s) = 0.066 \sim 0.07$.

Data availability

OCAMS images and OLA data from the Orbital A, Detailed Survey, and Orbital B phases of the OSIRIS-REx mission are available in the Planetary Data System at <https://sbn.psi.edu/pds/resource/orex/>. Measured dimensions and locations of craters and host boulders are available in Extended Data Tables 1 and 2, and Supplementary Information Table 1.

Code availability

The Small Body mapping tool is a publicly available mapping toolset that is available through the software's website: <http://sbmt.jhuapl.edu/>.

Methods Only References:

34. Britt, D.T., et al. Simulated asteroid materials based on carbonaceous chondrite mineralogies. *Meteoritics & Planetary Science* 54, 2067–2082 (2019).
35. Nakamura, A. M. Impact cratering on porous targets in the strength regime. *Planetary and Space Science* 149, 5–13 (2017).
36. Jutzi, M., Benz, W., and Michel, P. Numerical simulations of impacts involving porous bodies. I. Implementing sub-resolution porosity in a 3D SPH hydrocode. *Icarus* 198, 242–255 (2008).
37. Avdellidou, C., et al. Very weak carbonaceous asteroid simulants I: Mechanical properties and response to hypervelocity impacts. *Icarus* 341, 113648 (2020).
38. Poelchau, M.H., et al. The MEMIN research unit: Scaling impact cratering experiments in porous sandstones. *Meteoritics & Planetary Science* 48, 8–22 (2013).
39. Housen, K.R., and Holsapple, K.A. On the fragmentation of asteroids and planetary satellites. *Icarus* 84, 226–253 (1990).
40. Housen, K.R., and Holsapple, K.A. Scale Effects in Strength-Dominated Collisions of Rocky Asteroids. *Icarus* 142, 21–33 (1999).
41. Holsapple, K. A. On the Existence and Implications of Coupling Parameters in Cratering Mechanics. *Lunar and Planetary Science Conference* 14, 319 (1983)
42. Holsapple, K.A. The Scaling of Impact Processes in Planetary Sciences. *Annual Reviews of Earth and Planetary Sciences*, 21, 333–373 (1993).
43. Holsapple, K.A., and Housen, K.R. Craters From Impacts and Explosions, v 2.2.1. [Available at <http://keith.aa.washington.edu/craterdata/scaling/theory.pdf> Accessed July 2020]. (2017).
44. Hosapple, K. A. Catastrophic disruptions and cratering of solar system bodies: a review and new results. *Planetary and Space Science* 42, 1067–1078 (1994).

45. Suzuki, A.I., et al. Increase in cratering efficiency with target curvature in strength-controlled craters. *Icarus* 301, 1–8 (2018).
46. Leinhardt, Z.M., and Stewart, S.T. Collisions between Gravity-dominated Bodies. I. Outcome Regimes and Scaling Laws. *The Astrophysical Journal* 745, 79 (2012).
47. Leliwa-Kopystyński, J. et al. Impact cratering and break up of the small bodies of the Solar System. *Icarus* 195, 817–826 (2008).
48. Schenk, P., et al. The Geologically Recent Giant Impact Basins at Vesta’s South Pole. *Science* 336, 694–697 (2012).
49. Walsh, K. J. Rubble Pile Asteroids. *Annual Review of Astronomy and Astrophysics* 56, 593–624 (2018).
50. Bennett, C. et al. A High-Resolution Global Basemap of (101955) Bennu. *Icarus*, In Press (2020).
51. Barnouin, O.S. et al., Shape of (101955) Bennu indicative of a rubble pile with internal stiffness. *Nature Geoscience*, 12, 247–252 (2019).
52. Ernst, C. M. et al. The Small Body Mapping Tool (SBMT) for Accessing, Visualizing, and Analyzing Spacecraft Data in Three Dimensions. *Lunar and Planetary Science Conference* 49, 1043 (2018).
53. Lauretta, D.S. et al. OSIRIS-REx: Sample Return from Asteroid (101955) Bennu. *Space Sci. Rev.* 212, 925–984 (2017).
54. Barnouin, O.S., et al. Digital terrain mapping by the OSIRIS-REx mission. *Planetary and Space Science* 180, 104764 (2020).
55. Seabrook, J. A., et al. Global shape modeling using the OSIRIS-REx scanning Laser Altimeter. *Planet. Space Sci.*, 177, 104688 (2019).
56. Farrance, I. & Frankel, R. Uncertainty of Measurement: A Review of the Rules for Calculating Uncertainty Components through Functional Relationships. *Clinical Biochemistry Review* 33, 49–75 (2012).

ED Figure 1 | Examples of boulders with craters and the OLA profile of the craters. Boulders are outlined with dashed orange polygons. Craters are outlined with dashed white circles. The crater profile shown below each image corresponds to the dashed yellow line, with the letters A (start) and B (end) in the image indicating the direction of the corresponding profile (from left to right). **a)** Boulder 1 (image 20190328T191143S208_pol) has a circle-equivalent diameter of 2.9 m and an OLA-measured crater diameter of 1.21 ± 0.09 m. **b)** Boulder 2 (image 20190328T182010S618_pol) has a circle-equivalent diameter of 3.06 m and an OLA-measured

crater diameter of 1.24 ± 0.07 . **c)** Boulder 3 (image 20190329T205259S821_pol) has a circle-equivalent diameter of 4.24 m and an OLA-measured crater diameter of 1.60 ± 0.13 m. **d)** Boulder 4 (image 20190321T185825S567_pol) has a circle-equivalent diameter of 11.3 m and an OLA-measured crater diameter of 4.18 ± 0.47 .

ED Table 1 | Summary of OLA crater profile measurements for a subset of boulders that have crater size close to the maximum allowable before disruption. We tabulate updated values of crater dimensions using OLA digital terrain models of Boulders 1 to 7. For each boulder, we present the OLA-derived crater diameter, D , the uncertainty in D , $\sigma(D)$, the depth-to-diameter ratio, d/D , and the uncertainty in d/D , $\sigma(d/D)$.

ED Table 2 | Summary of boulders locations with flat faces that exhibit multiple impact craters on their surface. We tabulate the locations of boulders with multiple impact craters, the boulder's surface area, the number of craters measured on the boulder N_C , the diameter of the largest crater D_C , and the image used to make the size measurements.

Author Information:

The authors declare no competing financial interests. Correspondence and requests for materials should be addressed to R.-L.B. (rballouz@orex.lpl.arizona.edu).

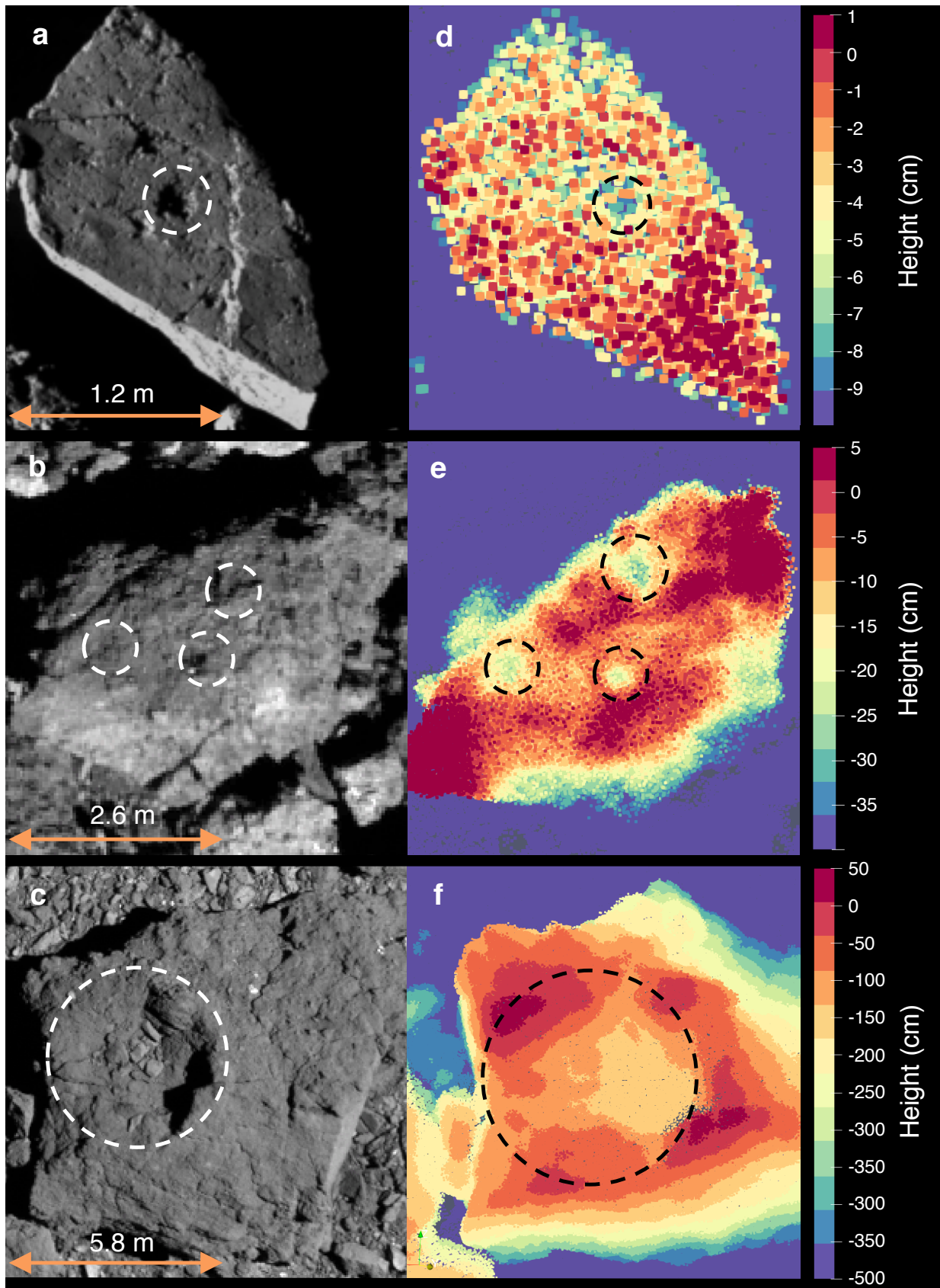


Figure 1

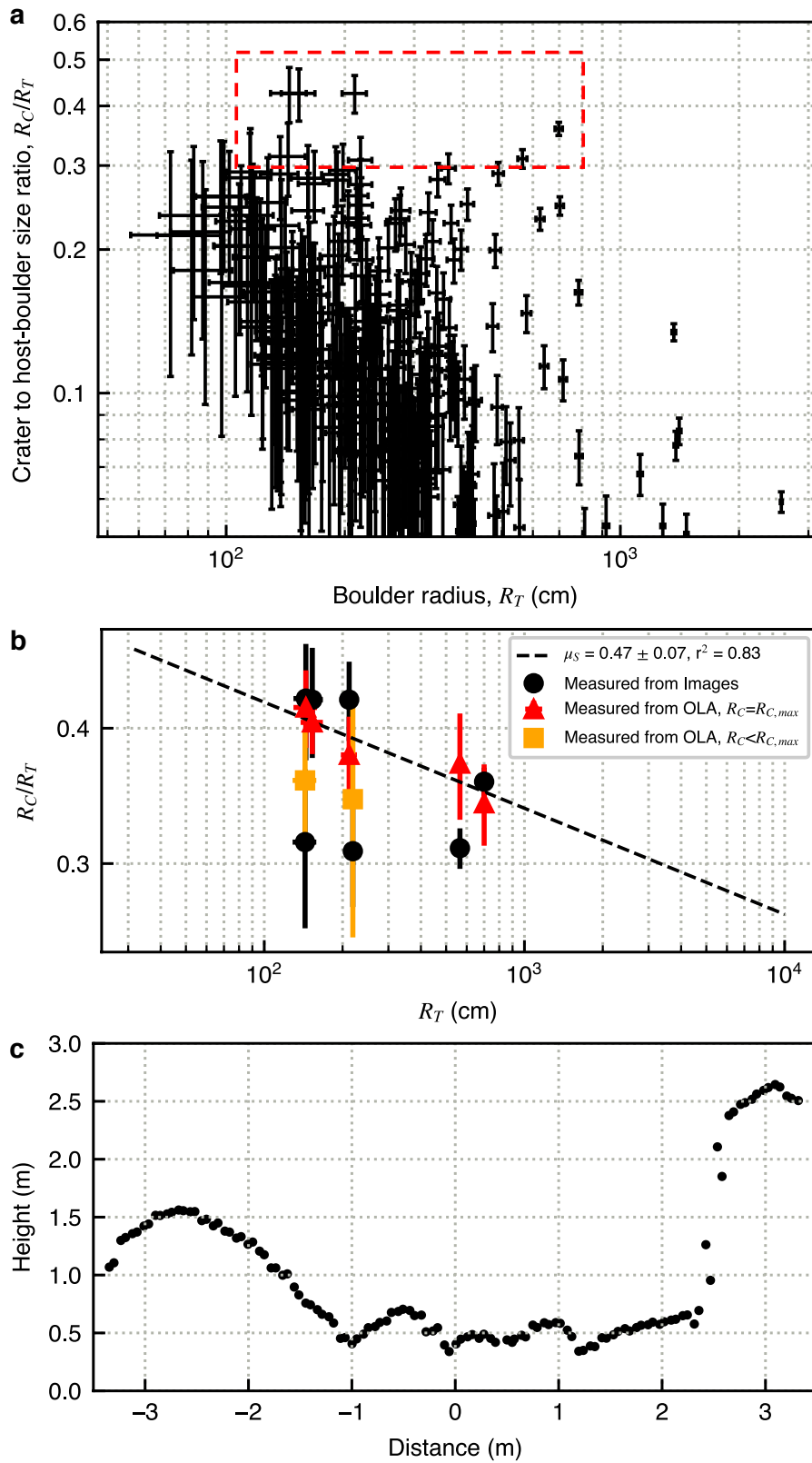


Figure 2

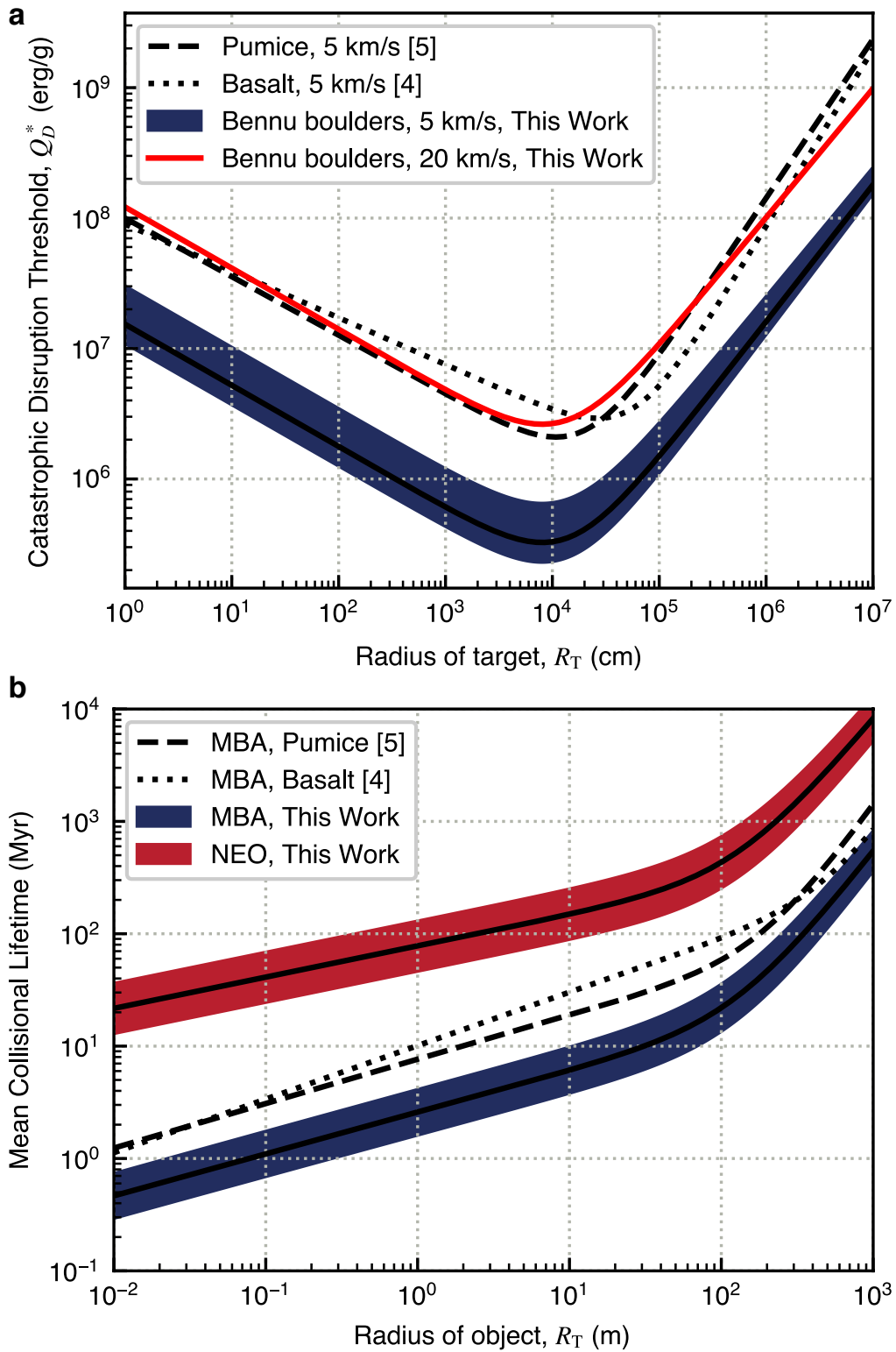


Figure 3

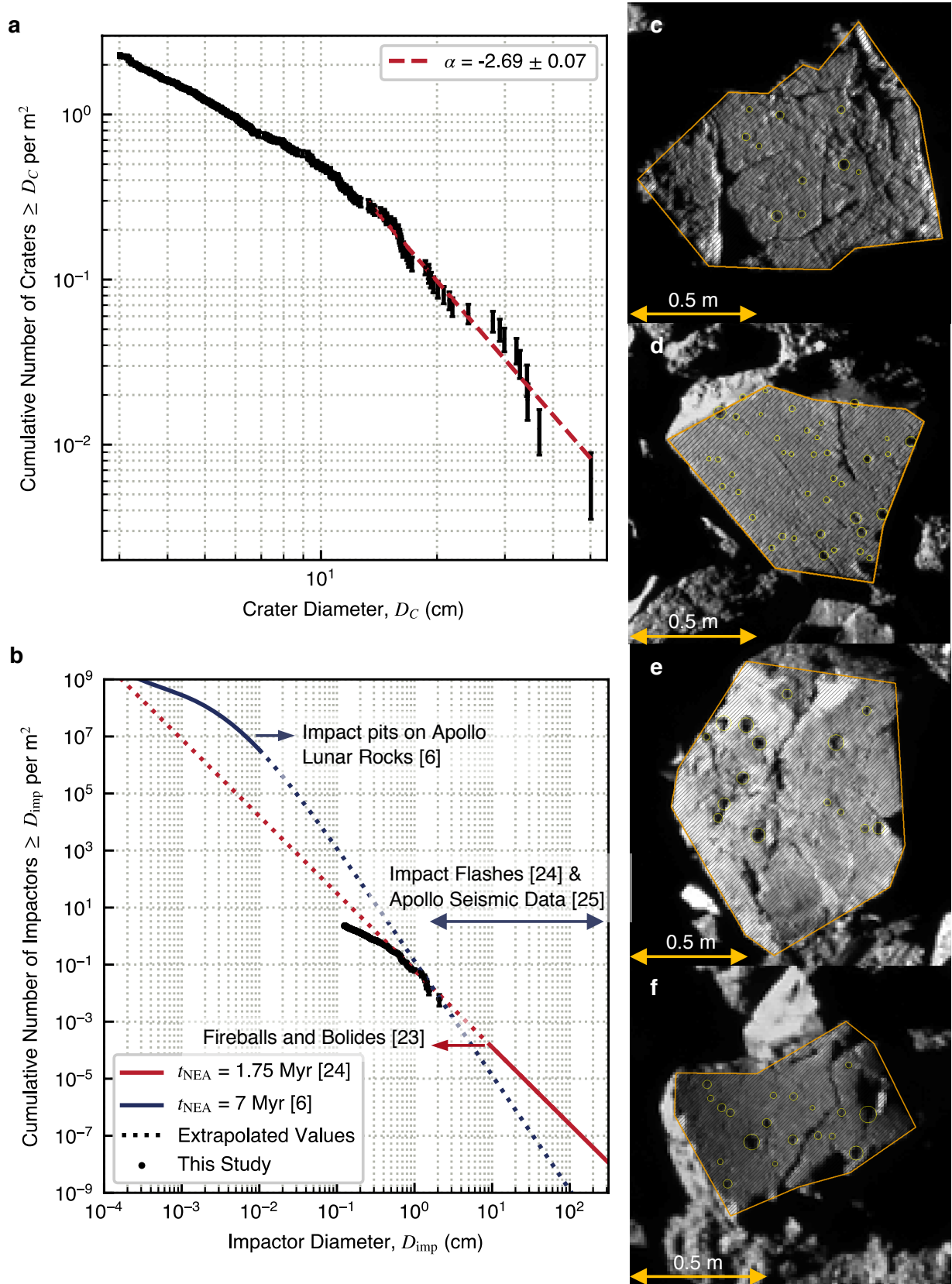
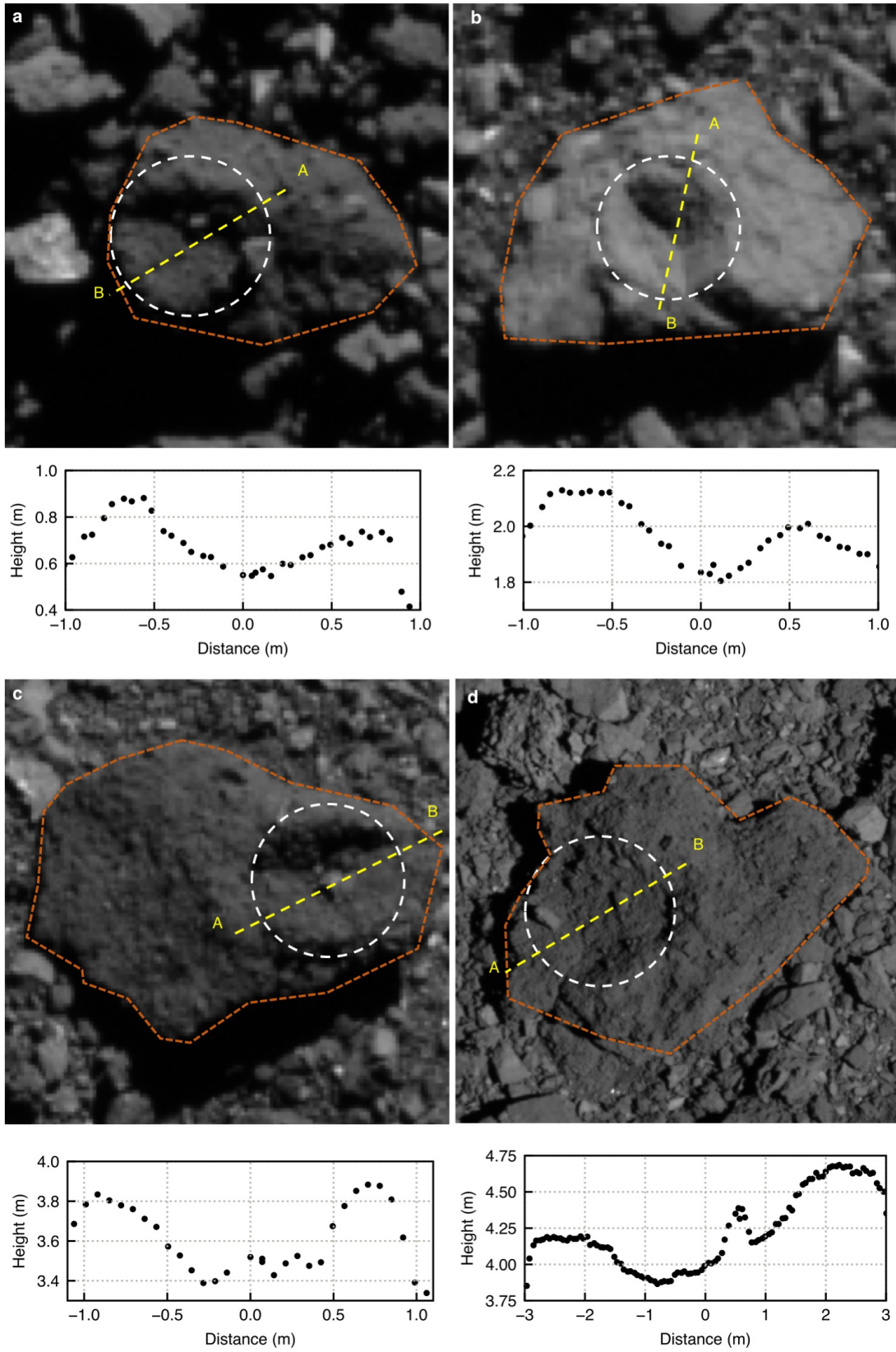


Figure 4



Extended Data Figure 1

Boulder #	OLA D (m)	OLA $\sigma(D)$ (m)	OLA d/D	OLA $\sigma(d/D)$
1	1.21	± 0.09	0.26	± 0.03
2	1.24	± 0.07	0.23	± 0.04
3	1.60	± 0.13	0.18	± 0.04
4	4.18	± 0.47	0.23	± 0.04
5	4.77	± 0.41	0.33	± 0.08
6	1.03	± 0.10	0.36	± 0.04
7	1.51	± 0.38	0.22	± 0.06

Extended Data Table 1

Lat (°)	Lon (°)	Boulder Area (m ²)	N _c	D _c max (cm)	Image Name
-35.3	316.3	3.74	62	32	20190703T044506S720_pol
2.7	120.4	1.92	37	19	20190703T070707S080_pol
-16.1	124.5	2.15	32	8	20190727T001538S345_pol
-11.9	281.6	1.38	22	8	20190702T074236S969_pol
-13.1	280.2	2.56	20	16	20190702T074236S969_pol
-27.3	309.8	1.29	20	20	20190717T035525S027_pol
-40.1	123.3	3.40	20	20	20190725T052037S178_pol
-5.9	251.7	0.94	15	10	20190720T120500S172_pol
5.2	271.5	0.74	12	6	20190706T020208S038_pol
-8	283.2	0.76	12	6	20190716T064549S614_pol
-43.3	10.7	1.60	11	16	20190712T112930S498_pol
-49.7	190.7	17.91	8	30	20190224T042628S037_pol
-76.9	55.5	10.81	8	19	20190723T111518S072_pol
-36.1	45.3	5.90	7	34	20190224T014627S831_pol
-4.5	262.8	0.94	7	5	20190720T115753S783_pol
65.9	149.3	3.03	6	28	20190226T220128S083_pol
-12.9	198.2	0.94	6	10	20190703T061019S015_pol
-27.7	156.2	11.12	5	17	20190224T002627S846_pol
-36.9	343.9	13.03	5	17	20190224T023128S611_pol
-64.6	61.9	5.07	5	34	20190226T232128S637_pol
-12.5	280.7	0.33	5	5	20190702T074236S969_pol
46.5	178.2	1.37	5	8	20190708T235419S989_pol
14.1	245.6	4.08	5	9	20190801T115754S186_pol
51.8	97.6	16.31	4	37	20190227T203627S733_pol
1.6	213.7	0.54	4	8	20190726T231144S159_pol
45.5	152	3.37	3	16	20190222T194128S519_pol
3.9	243.3	3.99	3	19	20190224T222628S636_pol
z	245.7	5.77	3	50	20190227T014128S206_pol
48	151.3	3.43	2	16	20190222T194128S519_pol
-50.7	191.6	3.97	2	16	20190224T042628S037_pol
-57.2	114.7	11.54	2	15	20190224T052628S198_pol
-64.9	191.8	4.23	2	16	20190224T092627S849_pol
68.3	194	1.31	2	11	20190224T092627S849_pol
-55.9	304.9	8.27	2	11	20190224T125142S753_pol
-42.9	157.2	0.35	2	3	20190705T230437S853_pol
55.4	246.1	2.26	1	14	20190227T014128S206_pol

Extended Data Table 2

Boulder #	Lat (°)	Lon (°)	R_c (m)	A_B (m ²)	R_c/R_T
1	-42.5	98.6	0.62	6.57	0.426
2	-33.6	178	0.65	7.35	0.425
3	13.3	116	0.9	14.10	0.425
4	3.7	170.8	1.65	100.10	0.310
5	-0.49	81.7	2.5	153.00	0.357
6	29.5	192	0.45	6.48	0.314
7	36.1	52.4	0.68	15.10	0.308
8	9.14	267	1.09	42.2	0.296
9	-41	117	0.58	12.3	0.293
10	-37	148	0.34	4.17	0.293
11	-42.4	77.3	1.42	75.5	0.289
12	-28.5	96.7	0.55	11.3	0.287
13	-54.7	148	0.39	5.91	0.287
14	-27.3	304	0.46	8.17	0.282
15	-40	110	0.32	4.15	0.281
16	-34.7	55.5	0.97	37.2	0.280
17	11.7	118	0.54	11.5	0.280
18	-52.4	147	0.6	15.1	0.274
19	22.3	298	0.46	8.8	0.274
20	46.4	353	0.56	14.4	0.259
21	-37	105	0.25	3.06	0.257
22	-45.4	88.8	0.25	2.95	0.257
23	56.2	196	1.02	52.7	0.249
24	30.2	273	0.32	5.11	0.249
25	-15.1	241	0.55	15.2	0.248
26	-27.5	87.7	1.74	155	0.247
27	-63.1	36.1	0.25	3.26	0.244
28	51.7	148	0.67	24.2	0.241
29	45.3	65	0.39	8.21	0.240
30	11.4	76.4	0.78	33.4	0.239
31	-70	140	0.28	4.27	0.236
32	10.7	319	0.19	2.15	0.234
33	11.5	24.4	0.5	14.5	0.233
34	-29.9	251	1.45	123	0.232
35	60.5	301	0.64	23.9	0.232
36	22.6	294	0.85	43.5	0.227
37	59.5	263	0.61	22.7	0.227
38	-24.8	97.2	0.25	3.74	0.227
39	10.1	326	0.46	13.1	0.226

40	-14.2	134	0.49	14.9	0.224
41	51.4	54.5	0.31	5.99	0.224
42	42.6	346	0.26	4.35	0.222
43	-27.2	45.8	0.16	1.64	0.217
44	-52.7	49.1	0.19	2.39	0.215
45	72.8	345	0.17	2.1	0.211
46	-42.6	144	0.41	12.2	0.209
47	13.2	159	0.7	35.1	0.208
48	23.3	179	0.59	25.6	0.205
49	-75.7	224	0.22	3.68	0.204
50	60.2	228	0.29	6.26	0.203
51	44.9	326	0.52	20.9	0.202
52	15.3	287	0.22	3.66	0.202
53	-17.6	280	0.79	48.9	0.200
54	-66.9	333	0.96	72.9	0.199
55	68.2	137	0.36	11.1	0.193
56	-38.2	136	0.24	4.67	0.193
57	11.1	84.8	0.23	4.47	0.192
58	-34.2	117	0.62	32.5	0.191
59	-38.7	153	0.72	45	0.190
60	-35.3	82.2	0.42	15.3	0.190
61	-10.4	335	0.33	10.4	0.183
62	2.53	276	0.3	8.33	0.182
63	-46.6	221	0.16	2.46	0.180
64	-34.6	84.2	0.44	18.7	0.179
65	40.1	146	0.56	30.5	0.178
66	-36.3	68.5	0.4	16.2	0.177
67	37.3	24.6	0.34	11.7	0.176
68	-14.8	282	0.51	27.3	0.171
69	-40.1	155	0.26	7.57	0.170
70	-9.15	301	0.21	4.77	0.170
71	9.62	16.2	0.52	29.6	0.169
72	-77.1	147	0.18	3.5	0.169
73	-38.6	143	0.24	6.8	0.166
74	-61	218	0.19	4.03	0.166
75	71.3	94.8	0.26	7.85	0.164
76	-26.9	337	1.28	193	0.163
77	-52	103	0.2	4.97	0.163
78	9.83	324	0.56	36.8	0.162
79	-27.3	111	0.27	8.84	0.161

80	15.9	9.56	0.39	18.9	0.160
81	-50.5	282	0.27	8.58	0.160
82	-65.4	134	0.15	2.98	0.158
83	-56.3	55	0.56	39.8	0.157
84	-23.5	78.2	0.23	6.82	0.157
85	-54.7	150	0.47	28.6	0.156
86	-4.61	245	0.24	7.43	0.156
87	48.2	43.9	0.18	4.22	0.155
88	41	51.6	0.36	16.8	0.154
89	13.7	335	0.42	23.7	0.153
90	42.6	186	0.37	18.5	0.151
91	-59.9	84.5	0.35	16.5	0.151
92	14.1	191	0.32	14.2	0.150
93	-22.4	147	0.41	23.2	0.149
94	39.8	15.9	0.26	9.4	0.148
95	-35.2	70.3	0.85	105	0.147
96	65.4	231	0.43	27	0.146
97	-64	136	0.28	11.4	0.146
98	24.4	87.9	0.35	18.1	0.144
99	-39.1	204	0.39	23.8	0.143
100	53	5.85	0.34	18.1	0.142
101	-3.24	5.44	0.2	6.35	0.142
102	1.18	22.7	0.31	15.6	0.141
103	-50.3	9.33	0.18	4.82	0.141
104	16.3	314	0.34	18.9	0.140
105	51.6	177	0.23	8.45	0.139
106	-11.1	330	0.17	4.8	0.139
107	15.6	21.9	0.66	70.7	0.138
108	57.3	233	0.51	42.6	0.137
109	41.9	303	0.32	16.8	0.137
110	-61	349	1.84	587	0.134
111	34.1	214	0.18	5.61	0.133
112	75.8	103	0.21	7.92	0.131
113	24.8	1.69	0.35	23.4	0.128
114	-40.4	53.9	0.19	6.55	0.128
115	-63.4	318	0.18	6.4	0.128
116	-38.3	41.1	0.18	5.95	0.127
117	-64.2	302	0.43	37.8	0.125
118	6.25	174	0.41	33.1	0.125
119	73.9	135	0.19	7.2	0.125

120	6.68	155	0.22	9.51	0.124
121	35.6	99.7	0.41	35.9	0.122
122	8.63	133	0.35	26.5	0.122
123	32.4	209	0.27	15.9	0.122
124	-3.23	203	0.34	25	0.121
125	-27.4	228	0.19	7.72	0.121
126	-64.2	351	0.16	5.58	0.121
127	-35.1	108	0.28	17.4	0.120
128	71.9	98.9	0.17	5.95	0.120
129	20	165	0.41	37.6	0.119
130	-58.9	184	0.16	5.76	0.119
131	-27.4	286	0.23	12	0.116
132	60.5	330	0.18	7.27	0.116
133	-26.9	133	0.16	5.98	0.116
134	-29	144	0.15	5.35	0.116
135	17.9	273	0.22	11.9	0.115
136	21.8	93.6	0.19	8.87	0.115
137	-50.1	136	0.73	129	0.114
138	32.1	36.8	0.26	16.7	0.114
139	-61.4	12.5	0.43	45	0.113
140	75.6	109	0.37	33.4	0.113
141	-20.4	208	0.3	22.8	0.113
142	-50.2	27.8	0.16	5.94	0.113
143	-17.1	223	0.41	42.4	0.112
144	-28.2	289	0.29	20.9	0.112
145	12.6	163	0.21	10.9	0.112
146	-47.5	180	0.22	12.9	0.111
147	-39	62	0.34	30.3	0.110
148	-48.1	225	0.18	8.63	0.109
149	-52.9	89.1	0.4	44.1	0.108
150	-29	288	0.22	13.4	0.108
151	49.7	123	0.77	161	0.107
152	9.01	11.1	0.43	50.8	0.107
153	-30	134	0.19	9.68	0.107
154	-0.58	323	0.17	8.23	0.107
155	19.2	160	0.17	7.87	0.107
156	12.7	12.6	0.34	32.1	0.106
157	-69	262	0.26	19.3	0.106
158	10	13.8	0.21	12.6	0.106
159	-40.5	32	0.3	27	0.102

160	41.8	45.4	0.22	14.1	0.102
161	38.4	330	0.39	45.8	0.101
162	-26.1	215	0.16	7.89	0.101
163	10.7	322	0.25	19	0.100
164	-23.2	123	0.37	43.1	0.100
165	4.56	302	0.32	33.5	0.099
166	54.6	354	0.15	7.52	0.099
167	-31.2	147	0.21	13.6	0.099
168	-73.7	97	0.19	11.1	0.098
169	52	50.6	0.38	47.1	0.097
170	-32.4	261	0.31	31.1	0.097
171	32.7	211	0.3	30.7	0.097
172	41.3	166	0.42	57.9	0.097
173	-67.8	308	0.15	7.57	0.097
174	-32.3	284	0.22	15.9	0.096
175	-55.2	9.17	0.23	17.6	0.096
176	63.1	21	0.4	56	0.095
177	-33.6	128	0.21	15.1	0.095
178	-52.7	299	0.25	22.1	0.094
179	-60.7	66.2	0.16	9.58	0.094
180	-30.6	154	0.15	8.27	0.094
181	10.2	169	0.19	13.3	0.094
182	10.9	11.1	0.21	15.5	0.093
183	27.6	146	0.45	74.5	0.093
184	-39.1	157	0.18	12.1	0.093
185	-27.6	268	0.31	37.4	0.090
186	-28.8	306	0.18	13.4	0.089
187	31.9	150	0.29	33.6	0.089
188	-7.02	223	0.18	13.5	0.088
189	-1.56	335	0.21	17.9	0.088
190	-47.9	42.4	0.19	14.2	0.088
191	27.7	278	0.26	27.4	0.088
192	38.7	238	0.19	15.1	0.087
193	24.5	21	0.29	36.4	0.085
194	35.3	192	0.15	10.5	0.085
195	3.4	27.9	0.22	21.4	0.084
196	18.9	18.4	1.18	625	0.083
197	7.64	120	0.16	11.8	0.082
198	-33.1	121	0.17	13.5	0.081
199	63.1	27.6	0.44	96	0.080

200	-19.7	146	0.25	29.6	0.080
201	-18.5	239	0.41	82.6	0.079
202	25.6	167	0.23	25.7	0.079
203	6.81	321	0.21	23	0.079
204	-22.1	236	0.25	32	0.079
205	42.6	127	1.08	601	0.078
206	-60.3	159	0.19	18	0.078
207	46.6	103	0.19	19.9	0.077
208	-80.3	134	0.19	19.6	0.077
209	-4.15	162	0.21	24.8	0.076
210	-23	93.2	0.16	13.2	0.076
211	-23.2	76	0.21	23.8	0.076
212	42.3	271	0.19	21	0.075
213	22.5	317	0.15	13.6	0.074
214	4.01	310	0.58	194	0.074
215	15	233	0.17	16.5	0.073
216	20.2	26.3	0.19	21.8	0.073
217	24.7	189	0.38	86.8	0.072
218	-1.57	186	0.19	22	0.072
219	-39.2	305	0.22	28.5	0.072
220	4.03	291	0.2	26.5	0.070
221	67.6	273	0.21	27.9	0.069
222	-7.71	32.2	0.24	39.5	0.069
223	58.9	127	0.22	32.3	0.069
224	-33.9	302	0.16	17	0.069
225	-12.8	11.6	0.19	24.6	0.068
226	-33.8	270	0.76	396	0.068
227	24.4	138	0.28	55.8	0.068
228	76	96.4	0.2	27.4	0.067
229	8.35	22.2	0.22	33.1	0.066
230	-34.8	273	0.17	19.9	0.066
231	60.3	211	0.2	28.8	0.066
232	44.2	121	0.27	53.1	0.065
233	38.8	318	0.21	33.3	0.065
234	11.9	124	0.27	54	0.064
235	48.6	132	0.17	22.4	0.064
236	43.6	343	0.2	31	0.063
237	-17.2	63.9	0.17	22.6	0.063
238	-44.4	291	0.2	34.2	0.060
239	-45.5	127	1.52	2060	0.059

240	57.5	242	0.23	48.8	0.059
241	7.8	307	0.29	80	0.057
242	32.1	110	0.16	27.4	0.056
243	-29.3	264	0.26	71.9	0.055
244	-38.6	262	0.68	516	0.053
245	-10.4	260	0.49	266	0.053
246	-19.6	78.6	0.22	53.6	0.053
247	52.2	344	0.29	96.7	0.052
248	21.3	143	0.21	50.1	0.052
249	-26.8	261	0.16	29.4	0.051
250	-83.3	202	0.75	680	0.051
251	38.5	150	0.2	50.9	0.050
252	57.6	171	0.2	53.1	0.049
253	25.1	358	0.39	207	0.048
254	24.2	156	0.22	73.8	0.045
255	5.44	38.8	0.18	57	0.043
256	15.2	146	0.16	47.1	0.041
257	-21.8	273	0.16	51.9	0.040
258	-52.9	170	0.31	223	0.037

Supplementary Information Table 1 | Dimensions of craters and their host boulders on the surface of Bennu. We tabulate the locations of boulders with craters and their dimensions based on shape model-projected images with pixel scales of 5 cm. We measure their largest crater radius R_C , the boulder areal extent A_B , and the ratio of the crater radius to the host boulder circle-equivalent radius R_C/R_T . We assume 3-pixel uncertainties (15 cm) for these measurements.